Supplemental Material — 2D ice from first principles: structures and phase transitions

Ji Chen,[1, 2, *] Georg Schusteritsch,[2, 3, 4] Chris J. Pickard,[2, 3, 4]

Christoph G. Salzmann,[5] and Angelos Michaelides[1, 2, 5, †]

[1]*London Centre for Nanotechnology,*

17-19 Gordon Street, London WC1H 0AH, U.K.

[2]*Thomas Young Centre, University College London,*

20 Gordon Street, London, WC1H 0AJ, U.K.

[3]*Department of Physics and Astronomy, University College London,*

Gower Street, London WC1E 6BT, U.K.

[4]*Department of Materials Science and Metallurgy, University of Cambridge,*

27 Charles Babbage Road, Cambridge CB3 0FS, U.K.

[5]*Department of Chemistry, University College London,*

20 Gordon Street, London, WC1H 0AJ, U.K.

Abstract

Here we show: I. More details of the methods and computational settings used; II. Additional structural and vibrational information of monolayer ice; III. Phase stability as a function of confinement width at different pressures; IV. Calculations using different methods to address the validity of our results; V. Enthalpies including zero point energy corrections; and VI. Coordinates for some of the most relevant structures identified.

I. METHODS

Our density functional theory (DFT) calculations were carried out using the Vienna Ab-initio Simulation Package (VASP) [1]. Periodic boundary conditions are applied in all dimensions. The simulation model is a slab model (Fig. S1), in which the 2D ice layer is extended in lateral dimensions by periodic boundary conditions. In the out-of-plane dimension the inclusion of a vacuum area (>10 Å) ensures the interactions between a 2D ice layer and its images are negligible. The confinement was introduced by two flat structureless walls with a width of w. The K-point mesh had a lateral separation between points larger than 0.03 Å^{-1}. Projector augmented-wave potentials were used with an energy cut-off of 550 eV [2]. The generalized gradient approximation was used with the Perdew-Burke-Ernzerhof (PBE) exchange correlation functional [3] in conjunction with the van der Waals correction of Tkatchenko and Scheffler [4].

In our study, we used the *ab initio* random structure search (AIRSS) method to achieve an unbiased searching of the configuration space for 2D ice [7, 8]. Initial stuctures were built with 2, 4, 6, 8, 10, 12, 18 and 24 water molecules per unit cell using AIRSS. The lateral pressure is defined as the average of the lateral stress tensor elements $P = \frac{1}{2}(\sigma_{xx} + \sigma_{yy})$. In our DFT calculations with periodic boundary conditions with a slab model containing vacuum the lateral stress tensor of a 2D ice layer is not a conserved quantity with respect to the choice of vacuum. In fact the conserved quantities are $\sigma'_{xx} \times L_z$ and $\sigma'_{yy} \times L_z$, where L_z is the length of the cell in the out-of-plane direction, σ'_{xx} and σ'_{yy} are the calculated lateral diagonal stress tensor elements for the slab/vacuum model. The lateral stress tensor for a 2D ice layer is defined as $\sigma = \sigma' \times L_z/h$, where we assign the layer height h equals the width of the confinement. The lateral stress tensor is diagonalized during the relaxation of the unit cell until both σ_{xx} and σ_{yy} are converged to the target pressure. The cell dimension perpendicular to the water slab was fixed during structure optimization. The water-wall interaction was described using a classical Morse potential. Parameters of the Morse potential were obtained by fitting to the quantum Monte Carlo results for water monomer adsorption on graphene (Fig. S2) [5]. Calculations were also performed with a Lennard-Jones confining potential. As shown below the Morse and LJ confining potentials give qualitatively the same results (section IV).

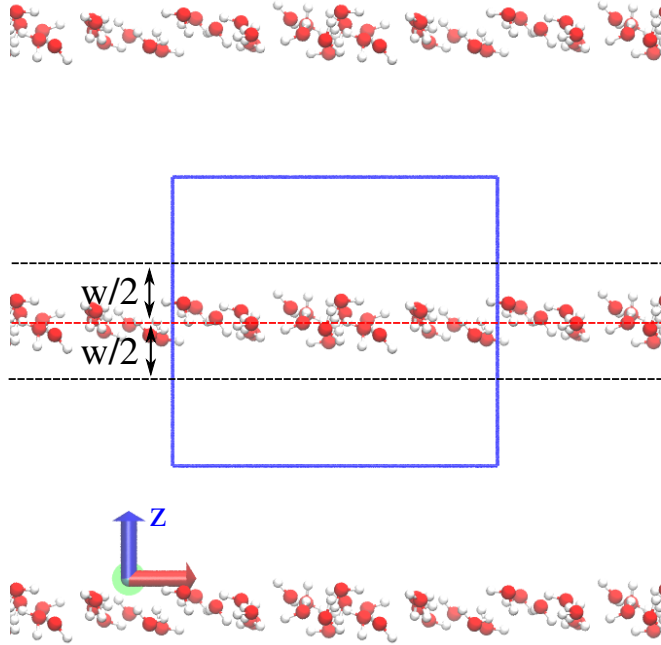In Fig. S3 we plot energy profiles of graphene-water-graphene slabs as a function of

FIG. S1. A typical unit cell for our DFT calculation of 2D ice with an empirical confinement. The red dashed line indicates the average height of all water molecules, the black dashed lines indicate the confined regime with a width of w.

the graphene interlayer spacing. Two sets of results which cover the density regime we are interested in are shown. It can be seen that the energy profile depends to some extent on the lateral density of water between the graphene layers. In the two structures used water molecules lie flat with all atoms located at the same height to graphene layers. Although the total energy depends to some extent on the orientation of water molecules, the sensitivity is much less than the influence of water density. With these two structures an estimate of the optimal interlayer spacing falls between 6.0 Å and 6.5 Å. Results at 6.0 Å and 6.5 Å are discussed in the paper and the dependence of the phase behavior in a wider range of confinement widths is shown in SI.III
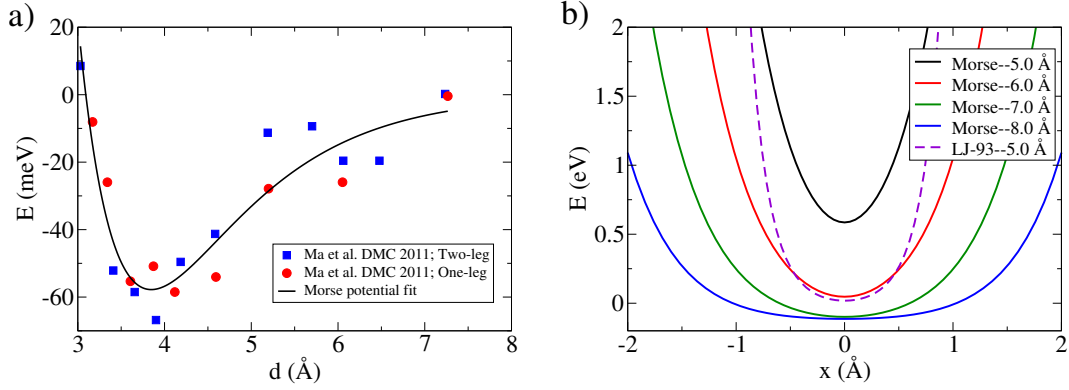
FIG. S2. (a) Fitted Morse potential of water-graphene interaction (black line). Blue squares and red circles are Diffusion Monte Carlo results from Ref. 5 for water in two orientations (so called two leg and one leg structure). $V(z) = D((1 - e^{-a(z-z_0)})^2 - 1)$, where z is the distance between the oxygen atom and the wall. $D = 57.8$ meV, $a = 0.92$ Å^{-1}, $z_0 = 3.85$ Å. (b) Potential energy of a water molecule between two walls with different wall separations. In addition to the profiles given for the Morse potential, the dashed line shows the potential energy profile of a Lennard-Jones 9-3 (LJ-93) potential with $\sigma = 3.0$ Å and $\epsilon = 21.7$ meV under 5.0 Å confinement [6].
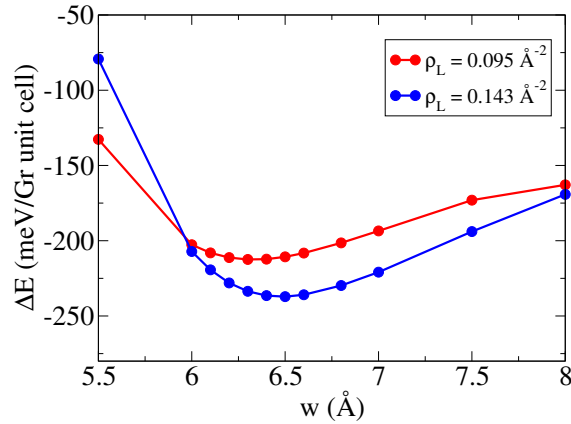

FIG. S3. Energy profile of graphene-water-graphene system as a function of interlayer separation. $\Delta E = (E_{total} - 2 * E_{graphene} - N_{H_2O} \times E_{H_2O})/N_c$, N_c is the number of graphene unit cells in one layer.

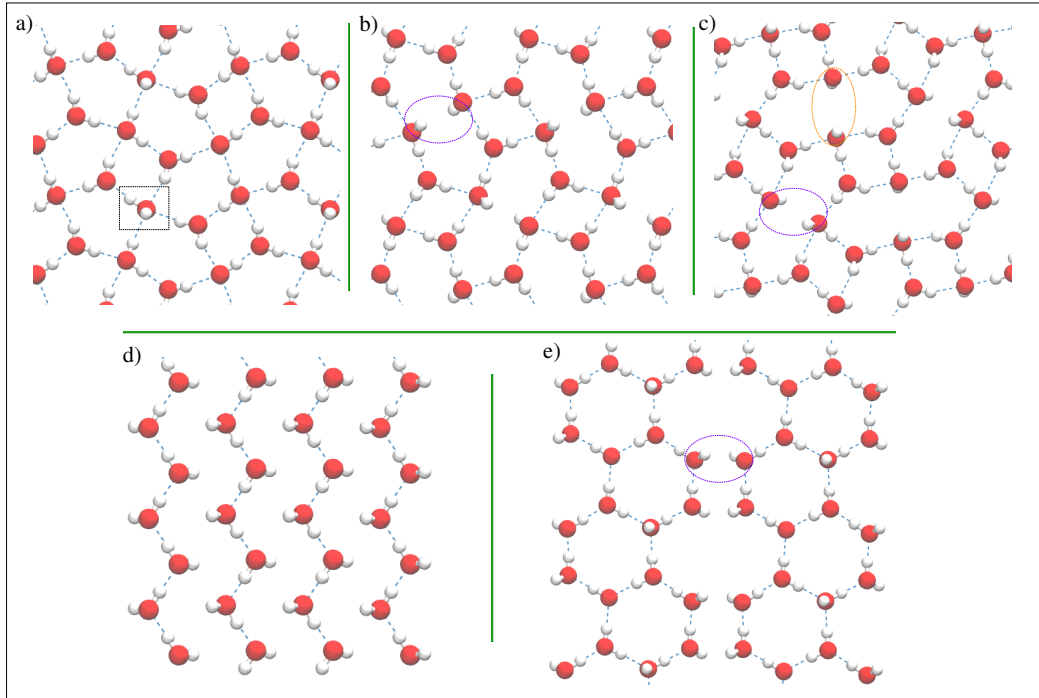## II. ADDITIONAL STRUCTURAL, ENERGETIC AND VIBRATIONAL INFOR-MATION

FIG. S4. Top views of the PT-I (a), the PT-II (b), the PT-III (c), the ZC (d), and the OHT (e) phases. The black box in panel (a) shows a water molecule which has three acceptor HBs. The Bjerrum D and L defects are highlighted with violet and orange ovals respectively.

Fig. S4 shows the structures of several other metastable phases identified. We dub these phases "PT-I" (Fig. S4a), "PT-II" (Fig. S4b), and "PT-III" (Fig. S4c). The PT-I, PT-II and PT-III phases differ from each other in the symmetry and the types of bonding they have (Table S1).

The PT-I phase has the $p2$ wall paper group symmetry for the oxygen lattice but the hydrogen atoms are disordered. Only hydrogen bonds and dangling OH bonds appear in the PT-I phase but some of the water molecules are five-fold coordinated (one dangling OH bond, one donor HB and three acceptor HBs), which is against the coordination character of oxygen atoms in the conventional ice.

The PT-II phase is an hydrogen ordered phase with the same wall-paper group symmetry

Structures	Symmetry of oxygen (water) lattice	Ring size	HB coordination	Defects
Hexagonal	*p6mm* (*p1*)	6	2D1A,1D2A	(1/2)DG
CT	*p4gm* (*p1*)	5	2D1A,2D2A,1D2A	(1/3)DG
f-SQ	*p4gm* (*p4gm*)	4	2D2A	NONE
ZC	*p2mg* (*p2*)	INF	1D1A	(1)DG
PT-I	*p2* (*p1*)	4,5	2D1A,2D2A,1D3A	(1/4)DG
PT-II	*p2* (*p2*)	4,5	2D1A,1D2A	(1/4)BJ-D
PT-III	*p2mg* (*p2*)	4,5	2D1A,1D2A	(1/8)BJ-L,(1/8)BJ-D,(1/4)DG
OHT	*p4mm* (*p1*)	4,6,8	2D1A,1D1A,1D2A	(1/4)BJ-D,(1/4)DG
b-SQ	*p4mm* (*p4gm*)	4	2D2A	NONE
b-RH	*p2mg* (*p1*)	4	2D2A	NONE

TABLE S1. Properties of stable and metastable structures. The wall paper group symmetry is determined using projections of the oxygen atoms (all atoms). In the HB coordination column "D" is donor HB and "A" is acceptor HB. In the defects column we use BJ-D and BJ-L to represent the Bjerrum D type and L type defects. Dangling OH bond (DG) is also considered in this column although it is not actually a defect. In the brackets we show how many "defects" there are in each water molecule.

(*p2*) for the oxygen lattice and the all atom lattice. All the water molecules have three HBs (either one donor two acceptor or one acceptor two donor) and the Bjerrum D type defects in one of the two types of water molecules.

The PT-III phase has a higher symmetry (*p2mg* for oxygen lattice). It consists of Bjerrum D and L defects as well as dangling OH bonds.

The structure in Fig. S4d forms one dimensional zigzag chains of HBs, thus we dub it "ZC". No bonds are formed between the neighbour chains with an oxygen-oxygen separation of *ca.* 3.8 Å. Each water molecule in the ZC phase has one donor HB, one acceptor HB and one dangling OH bond. It also has similar density and enthalpy to the PT phase.

We also identified a very low density metastable structure which we dub "OHT" considering the octagons, hexagons and tetramers we see from the top view of the structure (Fig. S4e). The OHT phase has a *p4mm* symmetry for the oxygen lattice and a disordered hydrogen network. We also find Bjerrum D type defects and dangling OH bonds in the OHT phase.

At the low pressure limit the enthalpies of all the metastable structures shown in Fig.

S4 are *ca.* 20-30 meV/water higher than the stable hexagonal and CT structure (Fig. S5). However the densities of these structures are quite different from one another, *e.g.* the OHT structure has a lower density than the hexagonal structure whereas most of the other structures have densities similar to the CT structure. The relative energy differences and densities are not sensitive to the size of confinement and the energy contributions of confinement are quite small.
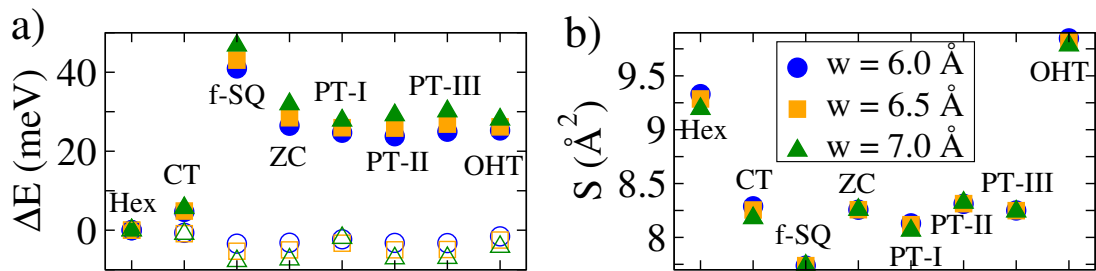
FIG. S5. (a) Relative enthalpies (filled symbols) and energy contributions from confinement (open symbols) of the stable and metastable structures at different confinements of 6.0 Å (blue circles), 6.5 Å (orange squares), and 7.0 Å (green triangles). (b) Lateral area per water molecule of the structures.

FIG. S6. Lateral molecular area (a) and out-of-plane buckling (b) of the structures as a function of pressure at 6.0 Å (solid lines) and 6.5 Å (dashed lines). The buckling is defined as the maximum height difference between oxygen atoms in a structure.

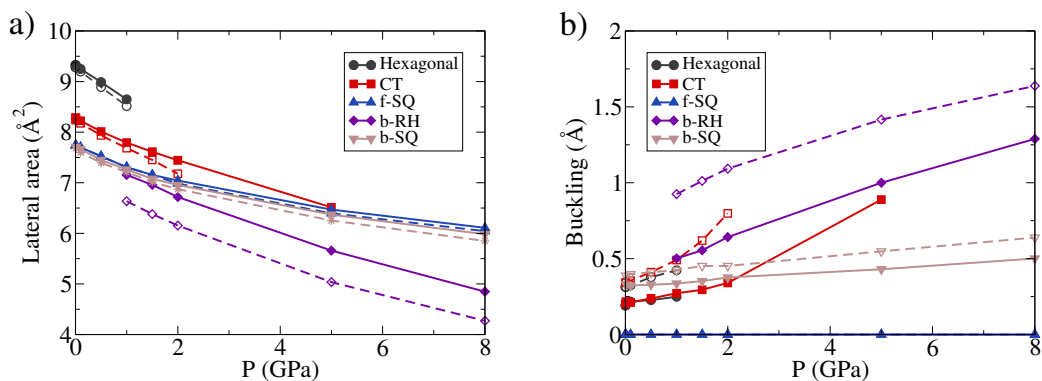In Fig. S6 we plot the lateral area and buckling as a function of lateral pressure. As we have shown in the main manuscript phase transitions of monolayer ice under 6.0 Å confinement happen at *ca.* 0.02 GPa (from hexagonal to CT), *ca.* 2 GPa (from CT to f-SQ), and *ca.* 4 GPa (from f-SQ to b-RH). The transitions all result in a drop of lateral area, thus a discontinuous increase of density. Under 6.5 Å confinement a transition from the CT phase to the b-RH is observed which is also accompanied by the sudden increase of density. The buckling changes continuously from the hexagonal to the CT phase, drops to zero for the f-SQ phase, and increases to a much larger buckling in the b-RH phase.
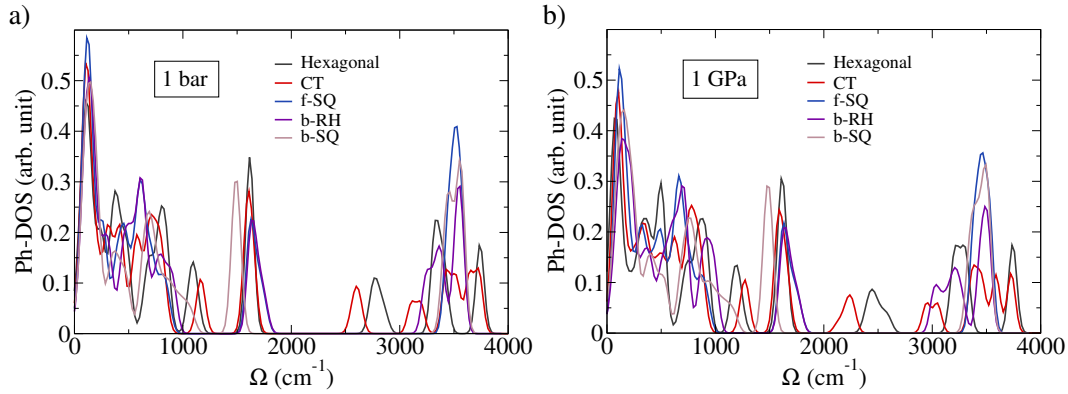

FIG. S7. Phonon density of states of the monolayer ice structures at 1 bar (a) and 1 GPa (b) with a 6.5 Å confinement.

Fig. S7 shows the phonon density of states of the structures. They were calculated within the harmonic approximation using the finite displacement method.

III. PHASE STABILITY AS A FUNCTION OF CONFINEMENT WIDTH AT DIF-FERENT PRESSURES

The influence of the confinement width on the predictions of the stable monolayer structures are shown in Fig. S8. At ambient pressure the enthalpy of the hexagonal phase remains the lowest up to a confinement width of *ca.* 7.3 Å, at which point the buckled (b-RH) phase becomes more stable. The CT phase is slightly less stable than the hexagonal phase by *ca.* 5 meV. As the pressure increases the transition from flat monolayers to buckled ice layers happens at smaller confinement widths. At 1 GPa the stability of the CT phase persists up to *ca.* 6.7 Å. At 3 GPa the f-SQ phase is stable at a confinement less than 6.1 Å.
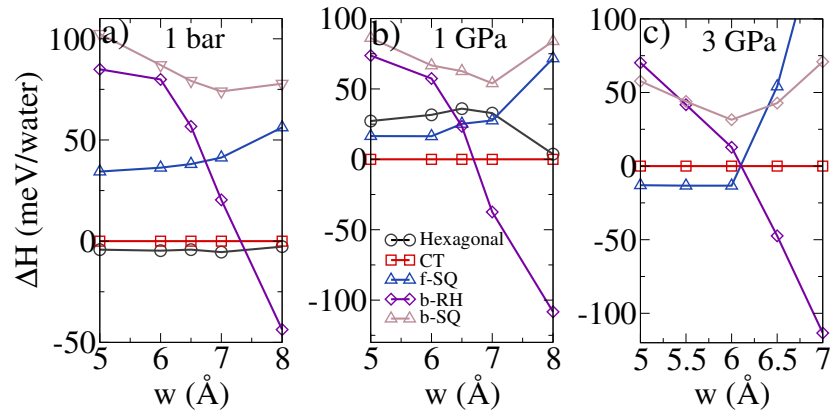

FIG. S8. Enthalpies of the water monolayer phases as a function of confinement width at 1 bar (a), 1 GPa (b), and 3 GPa (c). The definition of enthalpy is the same as in Fig. 2 of the main manuscript.

IV. CALCULATIONS USING DIFFERENT METHODS TO ADDRESS THE VALIDITY OF OUR RESULTS

Calculations using different exchange-correlation functionals were performed to test the validity of the key conclusions reached in this study. We now discuss: i) The sensitivity of results to the choice of exchange correlation functional and computational settings; ii) The difference with the DFT results reported in Ref. 9; iii) Calculations of 2D ice confined within actual sheets of graphene; iv) Calculations using a different confining potential; and v) Calculations using force field models.

i) The sensitivity of results to the choice of exchange correlation functional and computational settings.

We tested the validity of our results by doing a set of calculations using much higher settings (harder PAW potential, higher cutoff and denser K-point mesh). This shows that the errors are less than 10 percent of energy differences (Table S2).

We further performed calculations using different functionals to compare the enthalpies of the hexagonal, the CT and the f-SQ phases at ambient pressure and 6.5 Å confinement [3, 4, 10–14]. At this condition, all the calculations except PBE agree that the hexagonal phase and the CT phase are close in enthalpy. The square structure is less stable than the hexagonal structure in all calculations. In PBE van der Waals forces are not taken into account, leading to an underestimation of the stability of high density ice structures with respect to the low density ones [15, 16]. Here we can see that with the inclusion of van der Waals interactions the enthalpy difference between the high density f-SQ structure and the low density hexagonal structure becomes smaller, similar to the trend observed upon going from ice I to ice VIII [15, 16]. The value predicted by different van der Waals functional varies and without a benchmark study it is not straightforward to tell which one is more accurate. However, as we can learn from previous studies, inclusion of van der Waals interactions on GGA functionals usually change "underestimation" to "overestimation", especially for the PBE-vdW functional [13]. Therefore we speculate that at ambient pressure the f-SQ structure is less stable than the hexagonal and CT structures by a value between the prediction of PBE and the various van der Waals functionals, i.e. *ca.* 20 to *ca.* 50 meV/H_2O. In the future benchmark studies with more accurate electronic structure methods such as quantum Monte Carlo are highly desirable to substantiate the conclusions reached with

DFT.

H-H$_{hexagonal}$ (meV/H$_2$O)	CT	f-SQ
PBE+vdW(TS) [4]	4.9 (5.1)	43.1 (38.8)
PBE+vdW(TS)+ZPE [4]	1.8	42.6
PBE [3]	18.9	67.4
optB86b-vdW [13, 14]	3.4	16.3
HSE+vdW(TS) [4, 10, 12]	3.1	30.8
PBE-vdW [11]	-8.6	6.1

TABLE S2. Enthalpy differences between the hexagonal phase, the CT phase, and the f-SQ phase at ambient pressure and 6.5 Å confinement using different methods. Results shown in brackets are calculated using hard PAW potentials, a 1000 eV energy cutoff, and a K-point mesh denser than 0.02 Å^{-1}. "+ZPE" means the energy differences are corrected with the inclusion of zero point energy. Positive values indicate that the hexagonal structure is more stable than the CT or f-SQ structures.

In Table S3 we show the CT/f-SQ and f-SQ/b-RH transition pressures at 6.0 Å confinement to see the dependence of transition pressure on the choice of functional. As expected, the different performance of van der Waals functionals on high and low density ice structures results in a different transition pressure from the CT to the f-SQ phase. However, all three functionals predict a CT/f-SQ transition at a finite pressure in the order of 1 GPa. For the transition from the f-SQ to the b-RH, the transition pressure differences are much smaller with the different functionals as the HB network and density of the two structures are quite similar.

Transition pressure (GPa)	CT/f-SQ	f-SQ/b-RH
PBE+vdW(TS) [4]	1.9	4.2
optB86b-vdW [13, 14]	0.43	3.9
PBE-vdW [11]	0.51	3.8

TABLE S3. Transition pressure from CT to f-SQ (CT/f-SQ) and from f-SQ to b-RH (f-SQ/b-RH) at 6.0 Å confinement calculated using three different van der Waals functionals.

ii) The difference with the DFT results reported in Ref. 9.

It was reported in an arXiv preprint [9] that the square phase of monolayer ice is more stable than the hexagonal structure at all pressures. Even at ambient pressure it was suggested that the enthalpy of the square structure is lower by *ca.* 30 meV/H$_2$O [9]. This is different from our results where we see that the hexagonal monolayer ice phase is more stable at ambient pressure. We have identified two reasons for this discrepancy. First, in Ref. 9 the functional used is PBE-vdW, which favors the square structure the most among all the functionals tested (Table S2). Second, a small basis set was used in the SIESTA code calculations reported in Ref. 9, which results in a further overestimation of the relative stability of the square structure. We show this in Table S4 where we report our own SIESTA results. Compared with the more accurate basis sets such as $t\zeta + dp + p\prime$ and $q\zeta + tp + dp\prime$ or the plane wave DFT calculations using VASP, the $^{(P)}d\zeta + p$ basis set used in Ref. 9 overestimates the binding and underestimates the difference between the hexagonal and the square structures. Similar behavior has also been observed in more extensive tests of various basis sets for the binding of the water dimer and bulk ice structures [17]. With all these tests we are confident that the hexagonal structure is indeed more stable than the square structure at ambient pressure.

Methods \ energy (meV/H$_2$O)	E$_b$(f-SQ)	E$_b$(hexagonal)	ΔE
$^{(P)}d\zeta + p$ (SIESTA) [9, 18]	-451.2	-478.6	27.4
$t\zeta + dp + p\prime$ (SIESTA) [17]	-382.5	-430.5	48.0
$q\zeta + tp + dp\prime$ (SIESTA) [17]	-376.8	-425.9	49.1
Plane wave (VASP) [1]	-386.6	-459.0	72.4

TABLE S4. Binding energy and binding energy difference between the f-SQ and the hexagonal structure calculated using different methods. Single point total energy calculations are performed using PBE with structures optimized in a 6.5 Å confinement using the PBE+vdW(TS) method. We note that at ambient pressure the structures at different confinement widths or with different confinement potentials are almost identical as long as the confinement width is not too large, and the enthalpy difference mainly arises from the binding energy difference. Therefore, single point calculations can capture the differences resulted from different electronic structure methods. The main conclusion from this table is that the small $^{(P)}d\zeta + p$ basis set very poorly describes the energy difference between the hexagonal and the square structures.

iii) Calculations of 2D ice confined within actual sheets of graphene. To understand the influence a real graphene sheet would have on our results we have compared the energies of hexagonal and f-SQ structures at the low pressure limit. These structures are interesting to compare because they have quite different water molecule orientations; the hexagonal structure has dangling OH bonds pointing to the graphene sheets whereas in the f-SQ structure all the water molecules are in a plane parallel to the layer. We first calculated the energies of the hexagonal (Fig. S9a) and the f-SQ (Fig. S9b) 2D ice within two layers of distorted graphene sheets separated by 6.5 Å. The ice structures are those already obtained with our confining potential. The graphene lattices are distorted by < 2% to match the lattice of 2D ice. In Table S5 we report the energy difference between these two structures (data in column 1). We see the energy difference between the f-SQ and the hexagonal structure agrees quite well in two different methods. The other way to build a water/graphene structure is to keep graphene fixed at its equilibrium in plane lattice constant and distort the 2D ice sheet (Fig. S9c,d). In this case we re-optimise the structure of the 2D ice and then compare the relative energies of these re-optimised structures with the energies they would have if confined by our confining potential (Table S5, data column 2). We see that there is a difference ca. 10 meV/H_2O between the calculation using a confining potential and the full *ab initio* calculation. We conclude from these tests that although the presence of explicit graphene does alter the relative energies of the phases to some extent it does not alter any of the key conclusions of our study.

$\Delta E =$ E(f-SQ)-E(hexagonal) (meV/H_2O)	Graphene distorted	2D ice distorted
Morse potential confinement	43.1	25.9
Graphene Confinement	46.0	37.7

TABLE S5. Energy differences between the f-SQ structure and the hexagonal structure either confined by our regular Morse potential (derived from QMC) or confined by explicit graphene. E = $E_{total} - E_{graphene}$.

iv) Calculations using a different confining potential.

In previous force field simulations, a Lennard-Jones potential was usually used to describe the water-wall interaction. Here we test our calculations using the LJ-93 potential shown in Fig. S2b as the confinement. We see that to mimic the water graphene interaction, a quite different confinement size should be used. The main conclusions we discussed in the
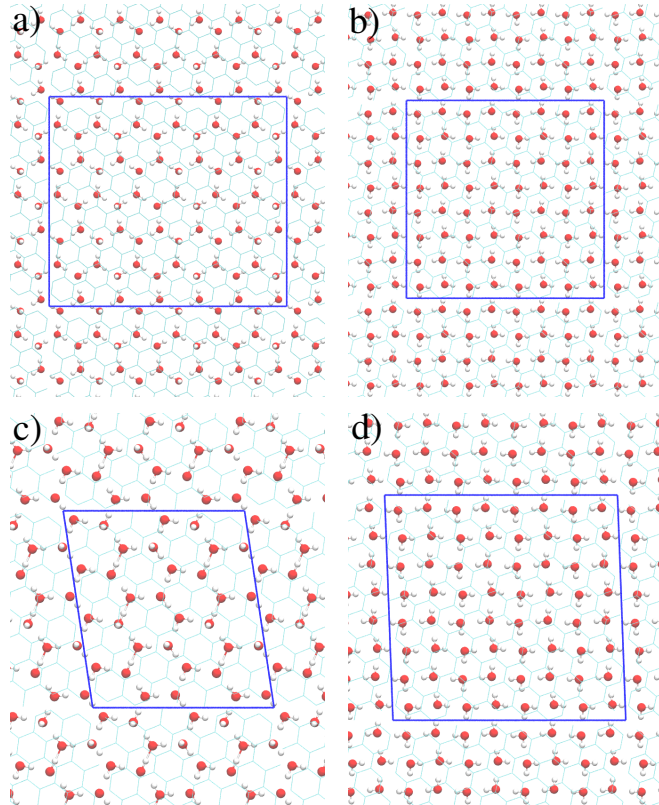
FIG. S9. a,b) Top view of 2D confined ice in two distorted graphene layers. c,d) The re-optimised structures of distorted 2D ice in undistorted graphene lattice.

paper can also be achieved by properly choosing the confinement size, *e.g.* the 5.0 Å LJ-93 potential results agree quite well with the 6.0 Å Morse-potential results (Fig. S10a).

v) Calculations using force field models.

Only the b-RH and f-SQ structures have been observed in force field simulations for monolayer ice in a smooth hydrophobic confinement [19–21]. The CT structure was only seen in double layer ice simulations [6]. The hexagonal structure was seen either as a double layer structure or in confinement with a hexagonal substrate structure as a template [6, 22, 23]. However the monolayer hexagonal and CT structures have not been reported in smooth confinement. In order to understand this, we calculated the enthalpies as a function of pressure using two widely used force fields, TIP4P/2005 [24] and SPC/E [25]. It is clear that the force fields and DFT predict qualitatively different results. Both force fields show that the b-RH is the lowest energy structure at all pressures and the f-SQ is the second lowest enthalpy structure (Fig. S10b,c). The CT and hexagonal structures are significantly
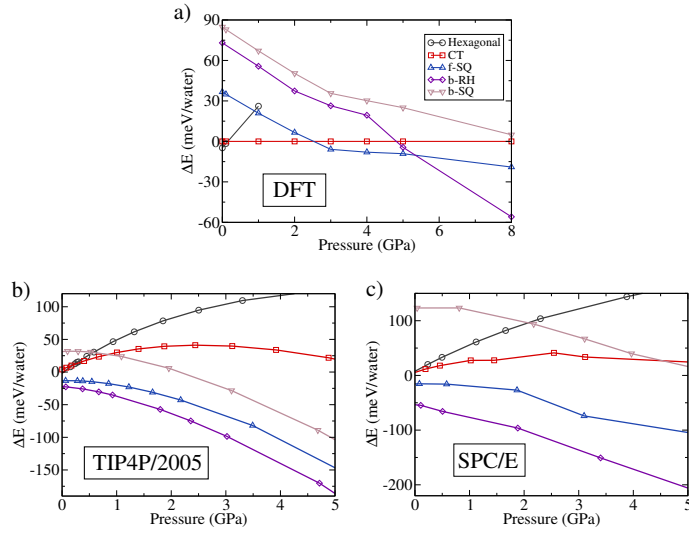
FIG. S10. Enthalpies of the water monolayer phases as a function of lateral pressure under 5.0 Å confinement using a LJ-93 potential described in Fig. S2b. The DFT data is with the PBE+vdW(TS) approach.

less stable at all pressures.

V. ENTHALPIES INCLUDING ZERO POINT ENERGY CORRECTIONS

In order to understand if zero point energy (ZPE) effects would change the conclusions reached here, we calculated the ZPEs using the harmonic approximation. The enthalpies are corrected by the ZPEs at different lateral pressures (Fig. S11). The ZPEs changes the transition point but the main conclusions reached in the paper are valid, *e.g.* at ambient pressure the enthalpy difference between the CT phase and the hexagonal phase is incredibly small: 5 meV without ZPEs and 2 meV with ZPEs.
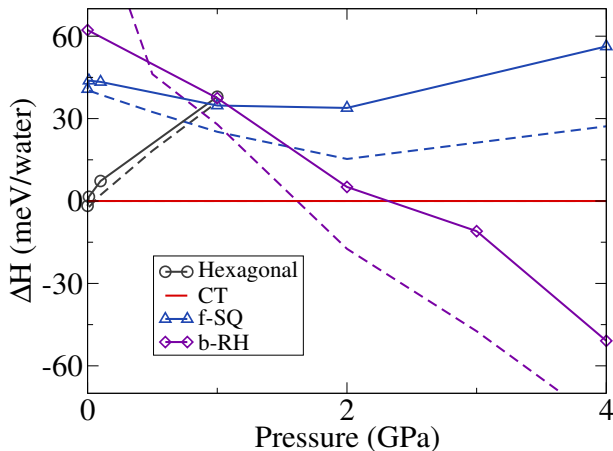
FIG. S11. Enthalpies with zero point energy (ZPE) corrections under 6.5 Å confinement (solid line with symbols). Relative enthalpies with respect to the CT phase is plotted. The dashed lines show the results without ZPEs.

VI. COORDINATES FOR SOME OF THE MOST RELEVANT STRUCTURES IDENTIFIED

In this section, coordinates for the hexagonal (#1), CT (#2), f-SQ (#3), b-RH (#4) and b-SQ (#5) obtained at ambient pressure with a 6.5 Å confinement are listed.

data_#1


```
_pd_phase_name                  'H   O                     '
_cell_length_a              9.17400
_cell_length_b              8.09685
_cell_length_c              15.00000
_cell_angle_alpha               90
_cell_angle_beta                90
_cell_angle_gamma               90
_symmetry_space_group_name_H-M       'P 1'
_symmetry_Int_Tables_number           1

loop_
_symmetry_equiv_pos_as_xyz
 'x, y, z'

loop_
  _atom_site_label
  _atom_site_occupancy
  _atom_site_fract_x
  _atom_site_fract_y
  _atom_site_fract_z
  _atom_site_adp_type
  _atom_site_B_iso_or_equiv
  _atom_site_type_symbol
  H1      1.0   0.699594    0.543205    0.492978    Biso  1.000000 H
  H2      1.0   0.614214    0.717110    0.494031    Biso  1.000000 H
  H3      1.0   0.300406    0.043205    0.507022    Biso  1.000000 H
  H4      1.0   0.385786    0.217110    0.505969    Biso  1.000000 H
  H5      1.0   0.851060    0.423601    0.574829    Biso  1.000000 H
  H6      1.0   0.957435    0.498075    0.503731    Biso  1.000000 H
  H7      1.0   0.148940    0.923601    0.425171    Biso  1.000000 H
  H8      1.0   0.042565    0.998075    0.496269    Biso  1.000000 H
  H9      1.0   0.800406    0.043202    0.492978    Biso  1.000000 H
  H10     1.0   0.885789    0.217104    0.494030    Biso  1.000000 H
  H11     1.0   0.199594    0.543202    0.507022    Biso  1.000000 H
  H12     1.0   0.114211    0.717104    0.505970    Biso  1.000000 H
  H13     1.0   0.351065    0.423607    0.425170    Biso  1.000000 H
  H14     1.0   0.457436    0.498079    0.496270    Biso  1.000000 H
  H15     1.0   0.648935    0.923607    0.574830    Biso  1.000000 H
  H16     1.0   0.542564    0.998079    0.503730    Biso  1.000000 H
  O1      1.0   0.602398    0.595686    0.498302    Biso  1.000000 O
  O2      1.0   0.397602    0.095686    0.501698    Biso  1.000000 O
  O3      1.0   0.862975    0.431765    0.510443    Biso  1.000000 O
  O4      1.0   0.137025    0.931765    0.489557    Biso  1.000000 O
  O5      1.0   0.897604    0.095680    0.498299    Biso  1.000000 O
  O6      1.0   0.102396    0.595680    0.501701    Biso  1.000000 O
  O7      1.0   0.362976    0.431769    0.489556    Biso  1.000000 O
  O8      1.0   0.637024    0.931769    0.510444    Biso  1.000000 O
```

data_#2

_pd_phase_name   'H O   '
_cell_length_a   9.95974
_cell_length_b   9.94506
_cell_length_c   15.00000
_cell_angle_alpha   90
_cell_angle_beta   90
_cell_angle_gamma   89.99287
_symmetry_space_group_name_H-M   'P 1'
_symmetry_Int_Tables_number   1

loop_
_symmetry_equiv_pos_as_xyz
 'x, y, z'

loop_
  _atom_site_label
  _atom_site_occupancy
  _atom_site_fract_x
  _atom_site_fract_y
  _atom_site_fract_z
  _atom_site_adp_type
  _atom_site_B_iso_or_equiv
  _atom_site_type_symbol
  H1   1.0   0.061737   0.174838   0.496521   Biso 1.000000 H
  H2   1.0   0.900693   0.171397   0.501272   Biso 1.000000 H
  H3   1.0   0.988240   0.953407   0.498511   Biso 1.000000 H
  H4   1.0   0.067640   0.814708   0.515726   Biso 1.000000 H
  H5   1.0   0.164650   0.581922   0.498672   Biso 1.000000 H
  H6   1.0   0.165495   0.422597   0.485079   Biso 1.000000 H
  H7   1.0   0.304222   0.924462   0.504400   Biso 1.000000 H
  H8   1.0   0.443879   0.005431   0.500255   Biso 1.000000 H
  H9   1.0   0.561692   0.325632   0.503476   Biso 1.000000 H
  H10   1.0   0.400643   0.329085   0.498741   Biso 1.000000 H
  H11   1.0   0.567638   0.685687   0.484196   Biso 1.000000 H
  H12   1.0   0.488226   0.547014   0.501446   Biso 1.000000 H
  H13   1.0   0.664638   0.918640   0.501231   Biso 1.000000 H
  H14   1.0   0.665499   0.077945   0.514918   Biso 1.000000 H
  H15   1.0   0.804171   0.576058   0.495549   Biso 1.000000 H
  H16   1.0   0.943848   0.495115   0.499710   Biso 1.000000 H
  H17   1.0   0.227674   0.256432   0.574808   Biso 1.000000 H
  H18   1.0   0.277929   0.149497   0.503769   Biso 1.000000 H
  H19   1.0   0.345276   0.708869   0.495260   Biso 1.000000 H
  H20   1.0   0.235775   0.756625   0.424799   Biso 1.000000 H
  H21   1.0   0.727726   0.244043   0.425233   Biso 1.000000 H
  H22   1.0   0.777941   0.351029   0.496245   Biso 1.000000 H
  H23   1.0   0.845239   0.791638   0.504669   Biso 1.000000 H
  H24   1.0   0.735696   0.743934   0.575106   Biso 1.000000 H

```
O1    1.0   0.982854   0.116111   0.502536   Biso  1.000000 O
O2    1.0   0.982870   0.852662   0.494781   Biso  1.000000 O
O3    1.0   0.109603   0.499535   0.501568   Biso  1.000000 O
O4    1.0   0.343942   0.014443   0.498206   Biso  1.000000 O
O5    1.0   0.482799   0.384353   0.497411   Biso  1.000000 O
O6    1.0   0.482887   0.647765   0.505180   Biso  1.000000 O
O7    1.0   0.609628   0.001067   0.498307   Biso  1.000000 O
O8    1.0   0.843917   0.486090   0.501797   Biso  1.000000 O
O9    1.0   0.237247   0.244847   0.510588   Biso  1.000000 O
O10   1.0   0.248428   0.745480   0.488821   Biso  1.000000 O
O11   1.0   0.737291   0.255677   0.489449   Biso  1.000000 O
O12   1.0   0.748367   0.755111   0.511088   Biso  1.000000 O
```

data_#3

```
_pd_phase_name                      'H  O                    '
_cell_length_a              5.56337
_cell_length_b              5.56343
_cell_length_c              15.00000
_cell_angle_alpha              90
_cell_angle_beta               90
_cell_angle_gamma               90
_symmetry_space_group_name_H-M      'P 1'
_symmetry_Int_Tables_number         1
```

loop_
_symmetry_equiv_pos_as_xyz
 'x, y, z'

loop_
  _atom_site_label
  _atom_site_occupancy
  _atom_site_fract_x
  _atom_site_fract_y
  _atom_site_fract_z
  _atom_site_adp_type
  _atom_site_B_iso_or_equiv
  _atom_site_type_symbol
```
H1    1.0   0.559637   0.763453   0.523069   Biso  1.000000 H
H2    1.0   0.736556   0.940374   0.476915   Biso  1.000000 H
H3    1.0   0.440363   0.236547   0.523069   Biso  1.000000 H
H4    1.0   0.263444   0.059626   0.476915   Biso  1.000000 H
H5    1.0   0.059637   0.736547   0.523069   Biso  1.000000 H
H6    1.0   0.236556   0.559626   0.476915   Biso  1.000000 H
H7    1.0   0.940363   0.263453   0.523069   Biso  1.000000 H
H8    1.0   0.763444   0.440374   0.476915   Biso  1.000000 H
```

O1	1.0	0.724952	0.775062	0.499993	Biso	1.000000	O
O2	1.0	0.275048	0.224938	0.499993	Biso	1.000000	O
O3	1.0	0.224951	0.724938	0.499993	Biso	1.000000	O
O4	1.0	0.775048	0.275062	0.499993	Biso	1.000000	O

data_#4

```
_pd_phase_name                    'H O                        '
_cell_length_a              5.22074
_cell_length_b              5.59951
_cell_length_c              20.00000
_cell_angle_alpha              90
_cell_angle_beta               90
_cell_angle_gamma              90.00002
_symmetry_space_group_name_H-M       'P 1'
_symmetry_Int_Tables_number          1

loop_
_symmetry_equiv_pos_as_xyz
 'x, y, z'

loop_
  _atom_site_label
  _atom_site_occupancy
  _atom_site_fract_x
  _atom_site_fract_y
  _atom_site_fract_z
  _atom_site_adp_type
  _atom_site_B_iso_or_equiv
  _atom_site_type_symbol
```

H1	1.0	0.475650	0.217714	0.537233	Biso	1.000000	H
H2	1.0	0.281312	0.037703	0.506176	Biso	1.000000	H
H3	1.0	0.975649	0.217712	0.462765	Biso	1.000000	H
H4	1.0	0.781313	0.037704	0.493821	Biso	1.000000	H
H5	1.0	0.024293	0.717713	0.462765	Biso	1.000000	H
H6	1.0	0.218630	0.537703	0.493821	Biso	1.000000	H
H7	1.0	0.718630	0.537703	0.506176	Biso	1.000000	H
H8	1.0	0.524293	0.717714	0.537233	Biso	1.000000	H
O1	1.0	0.464994	0.056313	0.518028	Biso	1.000000	O
O2	1.0	0.964994	0.056311	0.481969	Biso	1.000000	O
O3	1.0	0.034949	0.556312	0.481969	Biso	1.000000	O
O4	1.0	0.534949	0.556313	0.518028	Biso	1.000000	O

data_#5

_pd_phase_name   'H   O   '
_cell_length_a   5.53742
_cell_length_b   5.53742
_cell_length_c   20.00000
_cell_angle_alpha   90
_cell_angle_beta   90
_cell_angle_gamma   90
_symmetry_space_group_name_H-M   'P 1'
_symmetry_Int_Tables_number   1

loop_
_symmetry_equiv_pos_as_xyz
  'x, y, z'

loop_
  _atom_site_label
  _atom_site_occupancy
  _atom_site_fract_x
  _atom_site_fract_y
  _atom_site_fract_z
  _atom_site_adp_type
  _atom_site_B_iso_or_equiv
  _atom_site_type_symbol
    H1   1.0   0.603762   0.250000   0.393238   Biso 1.000000 H
    H2   1.0   0.250000   0.103762   0.356850   Biso 1.000000 H
    H3   1.0   0.750000   0.603763   0.356850   Biso 1.000000 H
    H4   1.0   0.896237   0.250000   0.393238   Biso 1.000000 H
    H5   1.0   0.396238   0.750000   0.393238   Biso 1.000000 H
    H6   1.0   0.750000   0.896237   0.356850   Biso 1.000000 H
    H7   1.0   0.250000   0.396237   0.356850   Biso 1.000000 H
    H8   1.0   0.103762   0.750000   0.393238   Biso 1.000000 H
    O1   1.0   0.250000   0.250000   0.384874   Biso 1.000000 O
    O2   1.0   0.750000   0.250000   0.365214   Biso 1.000000 O
    O3   1.0   0.750000   0.750000   0.384874   Biso 1.000000 O
    O4   1.0   0.250000   0.750000   0.365214   Biso 1.000000 O

* ji.chen@ucl.ac.uk

† angelos.michaelides@ucl.ac.uk

[1] G. Kresse and J. Furthmüller, Physical Review B **54**, 11169 (1996).

[2] G. Kresse and D. Joubert, Physical Review B **59**, 1758 (1999).

[3] J. P. Perdew, K. Burke, and M. Ernzerhof, Physical Review Letters **77**, 3865 (1996).

[4] A. Tkatchenko and M. Scheffler, Physical Review Letters **102**, 073005 (2009).

[5] J. Ma, A. Michaelides, D. Alfè, L. Schimka, G. Kresse, and E. Wang, Physical Review B **84**, 033402 (2011).

[6] J. C. Johnston, N. Kastelowitz, and V. Molinero, The Journal of Chemical Physics **133**, 154516 (2010).

[7] C. J. Pickard and R. J. Needs, Journal of Physics: Condensed Matter **23**, 053201 (2011).

[8] G. Schusteritsch and C. J. Pickard, Physical Review B **90**, 035424 (2014).

[9] F. Corsetti, P. Matthews, and E. Artacho, arXiv:1502.03750 [physics] (2015), arXiv: 1502.03750.

[10] J. Heyd, G. E. Scuseria, and M. Ernzerhof, The Journal of Chemical Physics **118**, 8207 (2003).

[11] M. Dion, H. Rydberg, E. Schröder, D. C. Langreth, and B. I. Lundqvist, Physical Review Letters **92**, 246401 (2004).

[12] J. Heyd, G. E. Scuseria, and M. Ernzerhof, The Journal of Chemical Physics **124**, 219906 (2006).

[13] J. Klimeš, D. R. Bowler, and A. Michaelides, Journal of Physics: Condensed Matter **22**, 022201 (2010).

[14] J. Klimeš, D. R. Bowler, and A. Michaelides, Physical Review B **83**, 195131 (2011).

[15] B. Santra, J. Klimeš, D. Alfè, A. Tkatchenko, B. Slater, A. Michaelides, R. Car, and M. Scheffler, Physical Review Letters **107**, 185701 (2011).

[16] E. D. Murray and G. Galli, Physical Review Letters **108**, 105502 (2012).

[17] F. Corsetti, M.-V. Fernndez-Serra, J. M. Soler, and E. Artacho, Journal of Physics: Condensed Matter **25**, 435504 (2013).

[18] J. Wang, G. Romn-Prez, J. M. Soler, E. Artacho, and M.-V. Fernndez-Serra, The Journal of Chemical Physics **134**, 024516 (2011).

[19] K. Koga and H. Tanaka, The Journal of Chemical Physics **122**, 104711 (2005).

[20] W.-H. Zhao, J. Bai, L.-F. Yuan, J. Yang, and X. C. Zeng, Chemical Science **5**, 1757 (2014).

[21] G. Algara-Siller, O. Lehtinen, F. C. Wang, R. R. Nair, U. Kaiser, H. A. Wu, A. K. Geim, and I. V. Grigorieva, Nature **519**, 443 (2015).

[22] S. Han, M. Y. Choi, P. Kumar, and H. E. Stanley, Nature Physics **6**, 685 (2010).

[23] A. L. Ferguson, N. Giovambattista, P. J. Rossky, A. Z. Panagiotopoulos, and P. G. Debenedetti, The Journal of Chemical Physics **137**, 144501 (2012).

[24] C. Vega, J. L. F. Abascal, M. M. Conde, and J. L. Aragones, Faraday Discussions **141**, 251 (2008).

[25] H. J. C. Berendsen, J. R. Grigera, and T. P. Straatsma, The Journal of Physical Chemistry **91**, 6269 (1987).